

# Double-Sided Arc Welding of AA5182-O Aluminum Sheet for Tailor Welded Blank Applications

*The conduction-mode double-sided arc welding process may be a viable alternative to traditional welding processes for aluminum tailor welded blanks*

BY J. A. MOULTON AND D. C. WECKMAN

## ABSTRACT

The viability of using the double-sided arc welding (DSAW) process, comprised of a plasma arc welding torch above and gas tungsten arc welding torch below the joint, to produce autogenous square welds between 1.0- and 1.5-mm-thick AA5182-O aluminum sheets for applications such as tailor welded blanks (TWB) has been studied. Visually acceptable complete-joint-penetration, conduction-mode DSA welds were produced with good cathodic cleaning of the oxide from both sides of the sheets over a wide range of welding speeds and powers from 10 mm/s when using 1.8 kW to 70 mm/s when using 4.6 kW. Transverse tensile tests showed that the weld strength was similar to the thinner base metal sheet; however, the displacement to failure was always less than the base metal. Hydrogen porosity was observed in the welds; however, this was significantly reduced by stainless steel wire brushing all affected surfaces prior to welding. SEM-EDS analysis and microhardness tests showed that there was no significant variation in composition and hardness between the base metal and weld metal. The DSAW process was found to be capable of producing welds with excellent visual quality at welding speeds that exceed those of traditional arc welding processes, thus demonstrating the potential for attaining the high productivity rates required for aluminum TWB applications.

## Introduction

Automotive manufacturers are coming under increasing regulatory pressure to continually improve the overall fleet mileage of their automobiles and to move toward use of more environmentally friendly fuels and energy sources such as hybrid and all-electric drive systems. Consequently, there is much interest in development and assessment of new materials and manufacturing technologies that will allow fabrication of lighter automotive bodies and structural components that continue to meet or exceed current safety and crash worthiness standards. For example, CO<sub>2</sub> laser welding of tailor welded blanks (TWB) of automotive steel sheets is a relatively new technology that has been shown to provide many advantages over the use of monolithic blanks including up to 30% weight savings for structural components (Refs. 1, 2). Tailor welded blanks are composite blanks made from combinations of different sheet steel and galvanized coating thicknesses that are joined together along butt joints using long, complete penetration square welds. Once welded, the TWB is stamped and formed into a structural component such as an inner door panel. Manufacturing of TWBs for the automotive industry requires welding processes capable of making high quality, complete joint penetration welds between two sheets of different thicknesses at high welding speeds (Ref. 1). This is a very demanding application

for any welding process, as not only must the weld have strengths comparable to the base metal, but it must also have sufficient ductility that it does not fail during drawing or stretching in the forming operation (Refs. 1, 2).

Further savings in automotive body weight can be realized by making TWBs from lighter aluminum alloys such as AA5754 and AA5182 for semistructural and internal closure applications and AA6111 for inner and external closure panels (Refs. 2, 3). These alloys have been used in the automotive industry for their good strength-to-weight ratio and forming characteristics; however, the high thermal conductivity and thermal expansion coefficient, low absorptivity, a tenacious aluminum oxide, and a sensitivity to hydrogen porosity make the welding of wrought aluminum alloys more challenging than the welding of traditional sheet steel alloys. To facilitate manufacturing of aluminum alloy TWBs in a high-speed production environment, new welding techniques must be identified and assessed. Recent studies suggest that electron beam welding (EBW), laser beam welding (LBW), and variable-polarity plasma arc welding (VPPAW) are the welding processes most likely to be successful for welding of aluminum alloy TWBs (Refs. 4, 5).

While CO<sub>2</sub> laser welding is commonly used to fabricate steel TWBs, aluminum has a low absorptivity at the CO<sub>2</sub> wavelength, which prevents absorption of the laser beam energy (Refs. 6, 7). Nd:YAG laser welding is preferred for welding aluminum alloys due to the higher absorptivity of aluminum at the Nd:YAG wavelength (Ref. 8). Deutsch et al. (Refs. 9, 10) reported that single-beam Nd:YAG laser welds on 1-mm-thick AA 5182-O aluminum alloy sheet exhibited spiky under-bead surfaces that they attributed to preferential vaporization of the Mg in the alloy and resultant keyhole instabilities. No combination of welding parameters could be found to eliminate this surface defect.

## KEYWORDS

Aluminum Alloys  
Double-Sided Arc Welding  
Hydrogen Porosity  
Tailor Welded Blanks

J. A. MOULTON (jamoulto@mecheng1.uwaterloo.ca) and D. C. WECKMAN (dweckman@uwaterloo.ca) are with Department of Mechanical & Mechatronics Engineering, University of Waterloo, Waterloo, Ont., Canada.

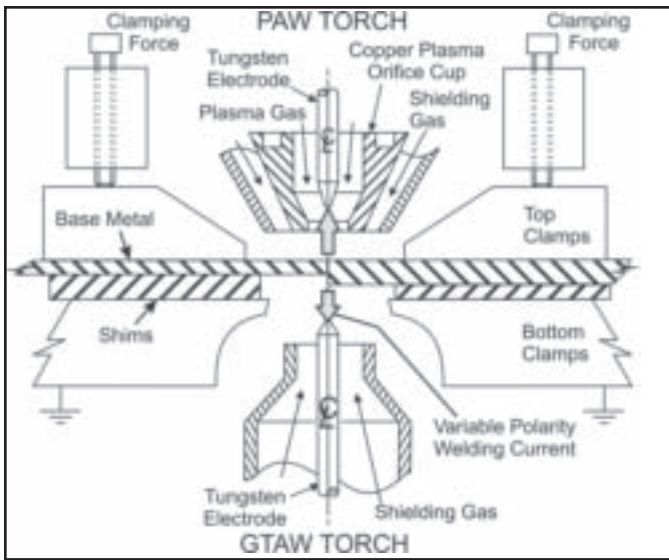


Fig. 1 — Schematic diagram of the DSAW process with a PAW torch above and a GTAW torch below the shimmed and clamped AA 5182-O aluminum sheet specimens.

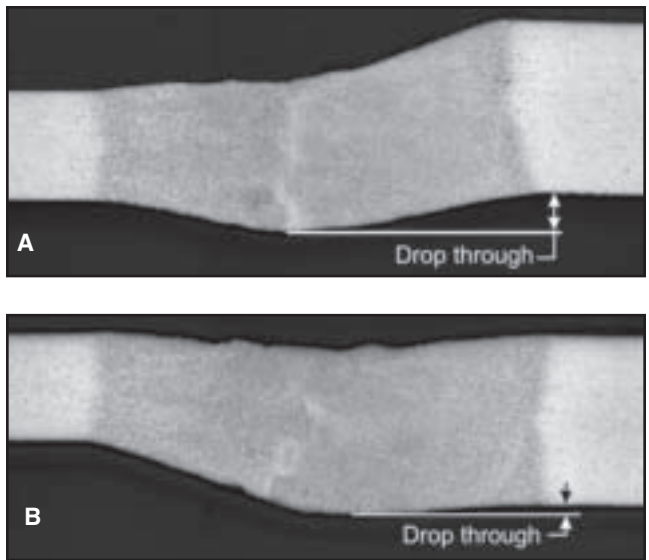


Fig. 2 — Weld cross-sectional geometry illustrating the difference in weld metal drop-through for welds produced between 1- and 1.5-mm-thick AA5182-O aluminum alloy sheets with the following: A — Bottom sheet surfaces aligned prior to welding; B — top sheet surfaces aligned prior to welding. (etch: Keller's (Ref. 29)).

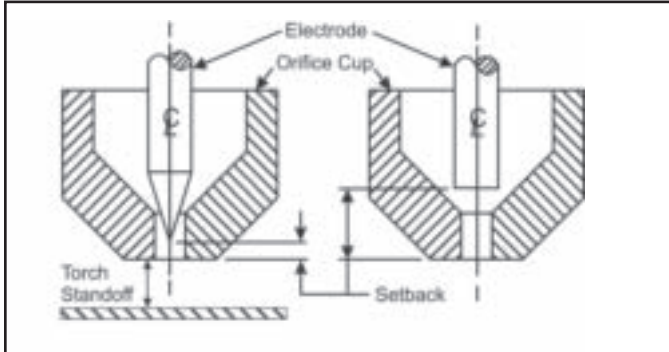


Fig. 3 — Schematic showing PAW torch standoff and electrode setback required to prevent electrode-to-orifice cup short circuiting for the following: A — An electrode ground to a 20-deg cone angle; B — a blunt electrode.

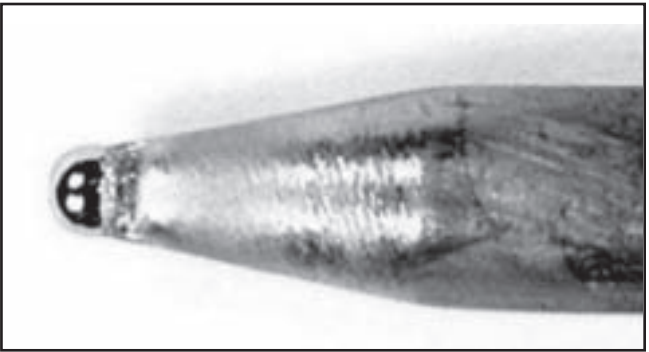


Fig. 4 — A 4.8-mm-diameter W-0.8% Zr electrode originally ground to a sharp 20-deg cone angle after VPPAW for only 1 min showing significant erosion and formation of a molten balled tip.

However, Deutsch et al. (Refs. 9, 10) and Punkari et al. (Refs. 11, 12) later showed that visually acceptable dual-beam Nd:YAG laser welds could be produced in 1-mm-thick 5182 and 5754 aluminum alloy sheet using total welding powers of 4.5 to 5.0 kW and travel speeds of 6 to 7.5 m/min.

The high energy density typical of laser beams has been reported to cause loss of alloying elements such as magnesium by vaporization during CO<sub>2</sub> laser welding (Refs. 13, 14). Moon and Metzbowner (Ref. 13) reported that the loss of magnesium in the weld metal contributed to a loss in strength in AA5456 aluminum alloy welds since this alloy derives its strength through solid solution strengthening from the magnesium. Porosity is another problem that has been reported in laser welding of aluminum alloys. Pores have been attributed to either hydrogen gas porosity or occluded vapor pores caused by keyhole in-

stabilities induced by the high vapor pressure of magnesium in the aluminum alloy (Refs. 10, 12, 14, 15).

The feasibility of applying VPPAW to the manufacture of TWBs has been investigated by Deutsch (Ref. 9) and Punkari (Ref. 11) using 1.6-mm-thick AA5182 and AA5754 aluminum sheet. A maximum welding speed near 3 m/min was reported, which was limited by the arc's ability to cathodically clean the surface oxide at higher speeds (Ref. 9). A stainless steel backing bar was required to control the under-bead geometry. This acted as an additional heat sink and restricted cathodic cleaning of the oxide to the top weld bead surface. Thus, oxide inclusions and incomplete fusion defects were sometimes evident on the underside of the weld. In addition, Punkari (Ref. 11) found that substantial welding power was required to prevent oxide inclusions, which resulted in wide welds with

nonsymmetric weld profiles and pronounced angular distortion of the sheets.

Double-sided arc welding (DSAW), shown schematically in Fig. 1, is a relatively new arc welding process that was patented by Zhang and Zhang (Ref. 16) in 1999. The DSAW process uses one welding power supply and two torches, frequently a plasma arc welding (PAW) and gas tungsten arc welding (GTAW) torch each connected directly to one of the power supply terminals. The torches are positioned on opposite sides of the work-piece such that the welding current flows from one torch through the workpiece to the opposite torch. The plates to be welded are grounded and not part of the electric welding circuit. Zhang et al. (Refs. 17–22) have examined the feasibility of using the DSAW process to make uphill, keyhole-mode welds in 6- to 12-mm thick plain carbon steel, stainless steel, or aluminum alloy plates.

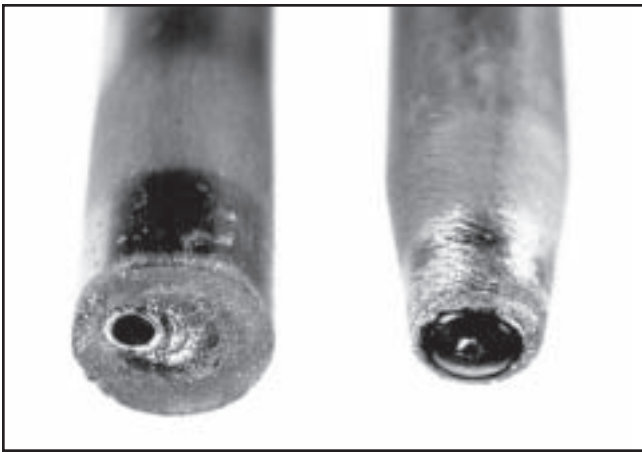


Fig. 5 — Images of 4.8-mm-diameter W-0.8% Zr electrodes after DSAW. The electrode on the right was ground to a 20-deg cone and truncated to 3.2 mm diameter and exhibits a larger molten spot after welding than the blunt electrode shown on the left.

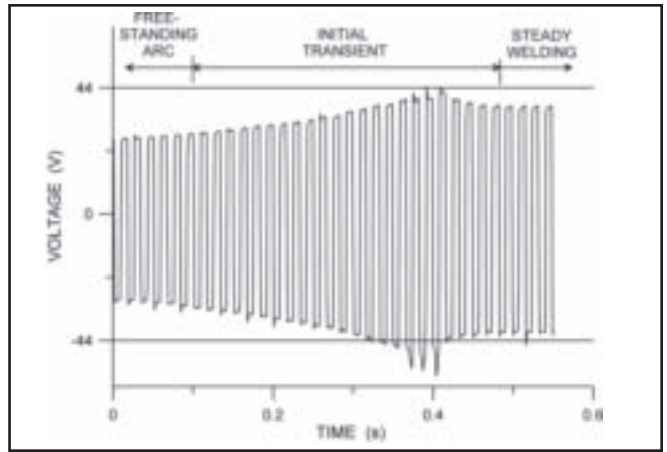


Fig. 6 — The normal start-up voltage transient in conduction-mode DSAW of aluminum sheet with a blunt electrode and 6.25-mm setback exceeded the maximum  $\pm 44$  V of the power supply and caused shutdown.

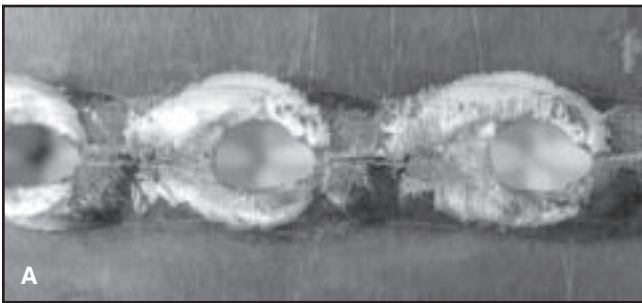
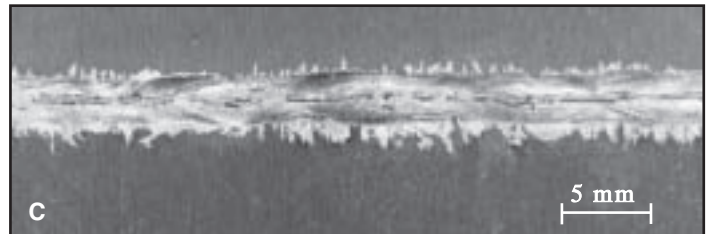
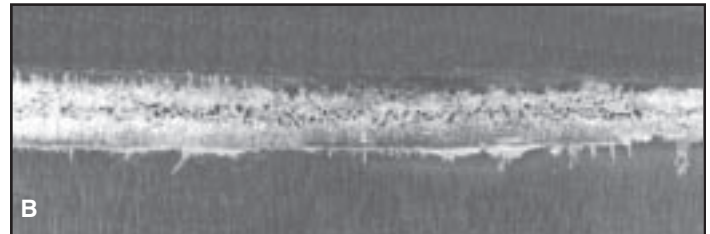


Fig. 7 — Top surfaces of welds made using a constant power of 2.6 kW and welding speeds; A — 10 mm/s with blowholes; B — good weld at 30 mm/s; C — inconsistent weld at 50 mm/s.



Kwon and Weckman (Ref. 23) recently examined the feasibility of using the DSAW process for conduction-mode welding of 1.2-mm-thick AA5182-O aluminum sheet. It was noted that the opposing welding torches successfully cleaned the oxide from both sides of the joint and produced visually acceptable welds at speeds up to 3.6 m/min. Through-thickness heating was more uniform with DSAW than with VPPAW allowing symmetric welds to be produced with minimal angular distortion of the sheets.

The demonstrated potential for welding aluminum sheet and the low capital cost compared to laser welding systems makes the conduction-mode DSAW process a potential candidate for welding aluminum TWBs; however, research to date has been limited to DSAW of similar thickness welds and the mechanical properties and quality of these welds have not been well characterized (Ref. 23). Therefore, the objective of the present study was

to examine the feasibility of applying the double-sided arc welding process to the manufacture of aluminum tailor welded blanks (Ref. 24). More specifically, it was of interest to identify the welding process parameters capable of producing high-quality welds between 1.0- and 1.5-mm-thick AA5182-O sheets in the butt-joint configuration such as might be required for TWB applications.

### Experimental Method

The material used in this study was nonheat-treatable AA5182-O aluminum alloy (cold rolled, annealed, and recrystallized) sheet in 1.0 and 1.5 mm thicknesses. The AA5182 alloy is solution strengthened by alloying with 4.5 wt-% Mg giving it good strength and reasonable ductility (Refs. 25, 26). This alloy is known for its good weldability (Refs. 26, 27). The aluminum sheet was sheared into specimens that measured 35 × 220 mm and 150 ×

430 mm. The larger specimens were used to produce transverse tensile specimens. All specimens were sheared to size perpendicular to the rolling direction, as this was found by Deutsch (Ref. 9) to provide the best cathodic cleaning of the aluminum oxide from the metal. Prior to welding, rolling lubricants and other contaminants were removed from the surface with acetone followed by a rinse with methanol. In a comparative study, a 200-mm (8-in.) bench grinder and stainless steel wire wheel with 0.3-mm-diameter wire were used to break up and remove the preexisting surface oxide from the area to be welded (Ref. 28).

A Miller® Aerowave® hybrid AC/DC constant current power supply was used to provide a balanced square-wave AC welding current at a frequency of 60 Hz, as previous DSAW research using this system showed that these settings provided the best cathodic cleaning of the aluminum oxide from both sides of the sheets (Ref.

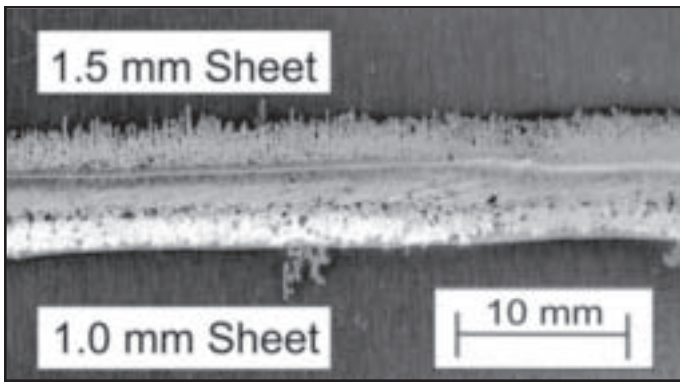


Fig. 8 — Preferential cathodic etching of the oxide that occurred on the thick sheet on the bottom surface only.



Fig. 9 — Transverse section of a DSA weld produced between 1.5- and 1-mm-thick sheets made using 2.6-kW welding power and 30 mm/s welding speed (etch: Beck et al. (Ref. 29)).

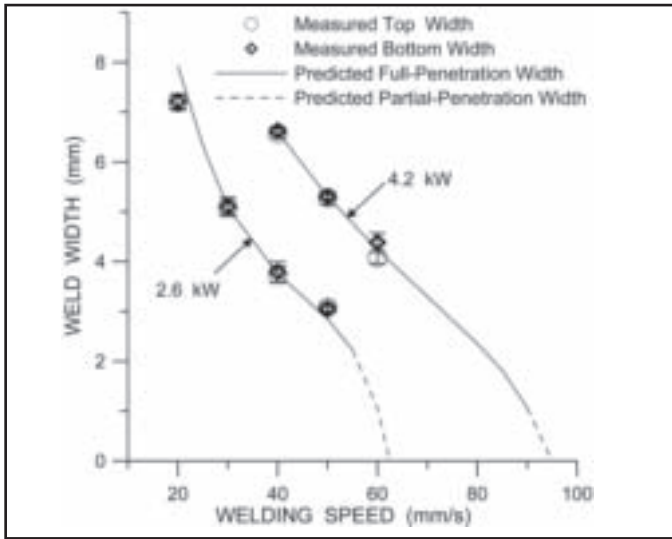


Fig. 11 — Measured and predicted top and bottom weld width vs. welding speed for total welding powers of 2.6 and 4.2 kW.

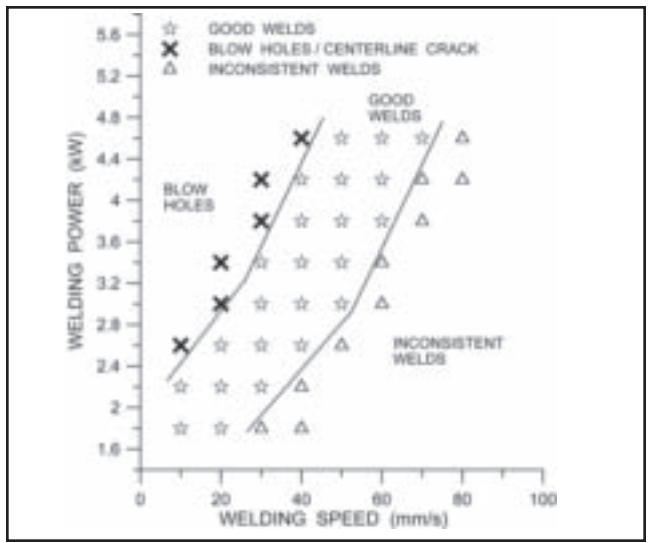


Fig. 10 — Range of visually acceptable welding conditions for DSAW of 1.0- to 1.5-mm-thick A5182 aluminum alloy sheet.

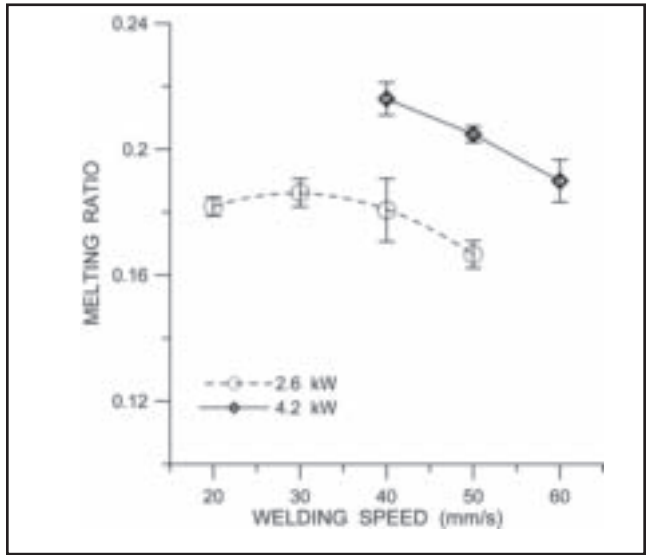


Fig. 12 — Melting ratio vs. welding speed for welds produced with total welding powers of 2.6 and 4.2 kW.

23). As shown schematically in Fig. 1, a Thermal Arc® WC100B, Model 300 PAW torch was positioned above the weld specimens and a Weldcraft® Model WP-27 GTAW torch was mounted below. A Thermal Dynamics® Thermal Arc® WC 100B plasma arc welding console was used to control the plasma and shielding gas flow rates and to provide pilot arc current for the PAW torch. This facilitated arc initiation between the two torches. The PAW torch was connected to the positive terminal of the power supply via the plasma arc

console, and the GTAW torch was connected to the negative terminal. Table 1 shows the preset PAW and GTAW torch parameters used in the experiments.

The clamping system shown schematically in Fig. 1 was used to hold the two specimens in the butt-joint configuration while they were moved on a carriage between the two torches at the desired welding speed. Prior to welding, the weld specimens were shimmed as shown in Fig. 1 so that the top surfaces of the specimens were flush. This was done to minimize

weld metal sag or drop-through.

A LabView 6.0-based control and data-acquisition system was used to control the welding carriage speed and to measure the welding current and voltage. The variable polarity welding current was measured using a LEM LT505-S Hall-effect current transducer and the voltage between the two torch electrodes was measured using a LEM LV100 Hall-effect voltage transducer. Voltage and current waveforms were sampled at 1 kHz and the data were used to calculate the root mean square

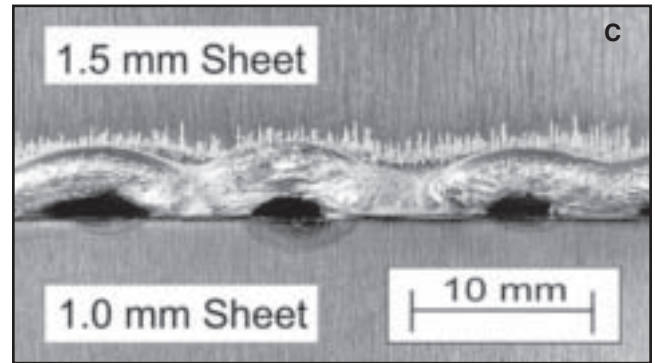
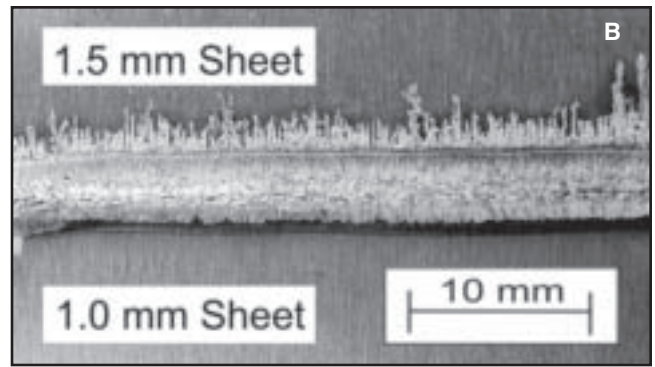
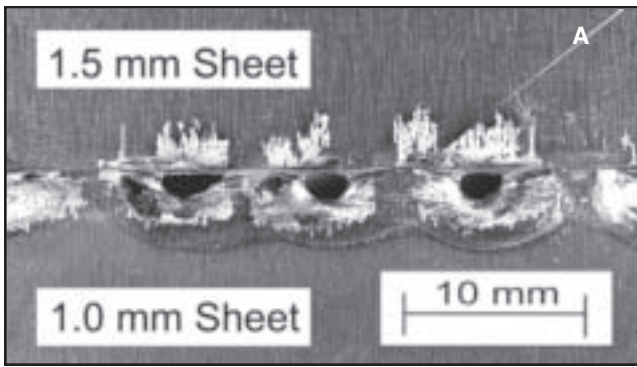


Fig. 13 — Top weld surfaces produced with 2.2-kW welding power at 30 mm/s with welding torches offset: A — 1 mm toward the thinner sheet resulting with blowholes in the thinner sheet; B — 1.0 mm toward the thicker sheet resulting in good quality welds; C — 2 mm toward the thicker sheet resulting in blowholes in the thicker sheet.

(RMS) values of current, voltage, power, and arc resistance.

Prior to each weld, the PAW pilot arc was started and then a free-standing arc of the desired peak welding current was created directly between the PAW and GTAW torches. Double-sided arc welds were then made by moving the weld specimens between the fixed torches at the desired welding speed. Initial experiments were performed to evaluate the effects of electrode tip geometry on electrode tip life. Following this, conduction-mode DSA welds were made at welding speeds ranging from 10 to 80 mm/s and welding powers ranging from 1.8 to 4.8 kW. Using the electrode gaps shown in Table 1, the total welding voltage was a dependent parameter that ranged between 32 and 35 V. A desired welding power was obtained by adjusting the peak welding current of the constant current power supply. Thus, peak welding currents ranging from about 40 to 150 A were used. The effect of torch position in the transverse direction relative to the weld joint was also evaluated. Finally, the effects of removing the oxide in the area of welding by stainless steel wire brushing on weld quality and welding speed were examined.

Metallographic examination and measurements of polished and etched specimens were performed using an Olympus™ optical microscope with an Image-Pro 4.5™ image analysis system. Two different reagents were used to etch the specimens: Keller's reagent was used to reveal the solidification microstructure, while Beck's reagent was used to reveal the grain structure (Ref. 29). Top and bottom weld width and weld area of each weld were measured. Mechanical properties were evaluated using Vickers microhardness tests and transverse tensile tests using the ASTM E8/E8M-08 (Ref. 30) Standard Sheet-Type Tensile Specimen geometry where the weld was located at the center of the modified 60-mm-long gauge length. Shims were used in the grips to avoid creating an induced couple due to the difference in sheet thicknesses and the sheet offset. The results were left as tensile load-displacement curves rather than stress-strain curves due to the three unique sec-

tions (1.0-mm-thick sheet, DSA weld and 1.5-mm-thick sheet) contained in the gauge length of the tensile specimen.

The melting ratio,  $MR$ , was calculated for each weld in order to determine the effects of welding process conditions on the overall energy coupling efficiency. The melting ratio is the fraction of the total incident power that is used to heat and melt the weld metal. The equation used to calculate  $MR$  is (Ref. 31)

$$MR = \frac{\rho \left[ C_p (T_{mp} - T_o) + \Delta H_f \right] L_w A_w}{L_w \left( \frac{P_L}{v_{ws}} \right)} \quad (1)$$

where  $L_w$  is the length of weld metal,  $A_w$  is the weld metal area,  $\rho$  is density,  $C_p$  is the specific heat,  $\Delta H_f$  is the latent heat of fusion,  $v_{ws}$  is welding speed,  $T_{mp}$  is the solidus temperature,  $T_o$  is room temperature, and  $P_L$  is the power from the power supply. The thermophysical properties of

A5182 used for this calculation were  $\rho = 2.65 \text{ Mg/m}^3$ ,  $C_p = 1.043 \text{ kJ/kg} \cdot \text{K}$ ,  $\Delta H_f = 397 \text{ kJ/kg}$ , and  $T_{mp} = 850 \text{ K}$  (Ref. 25). The values for  $\rho$  and  $C_p$  are averages of values between room temperature and  $T_{mp}$ .

## Results and Discussion

When welding TWBs of different sheet thicknesses, the sheets are normally aligned center to center and then welded so that drop-through or sagging of the weld pool during welding due to gravity does not cause problems with stacking of the welded blanks, excessive forming die

Table 1 — Constant Preset Welding Parameters Used for the PAW and GTAW Torches

Torch Parameter	PAW	GTAW
Electrode gap (mm)	9	4
Orifice diameter (mm)	3.2	—
Plasma gas	UHP Ar	—
Plasma gas flow rate (L/min)	0.45	—
Shielding gas	Ar	Ar
Shielding gas flow rate	19	19
Electrode composition	W-0.8% Zr	W-0.8% Zr
Electrode diameter (mm)	4.8	4.8
Electrode included angle (deg)	20	60
Electrode truncation (mm)	1.0	1.0

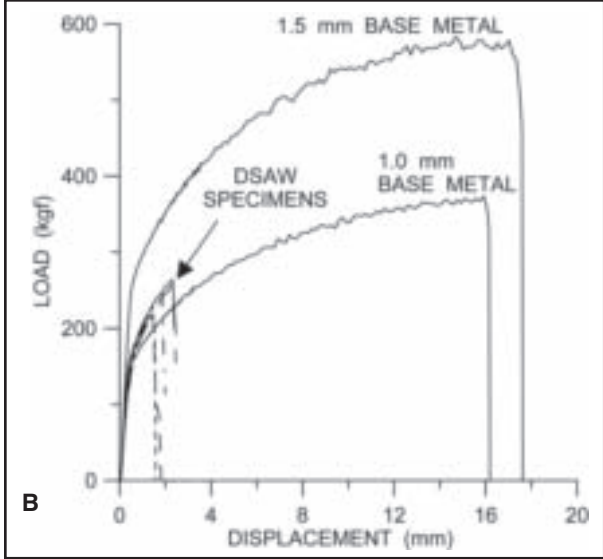
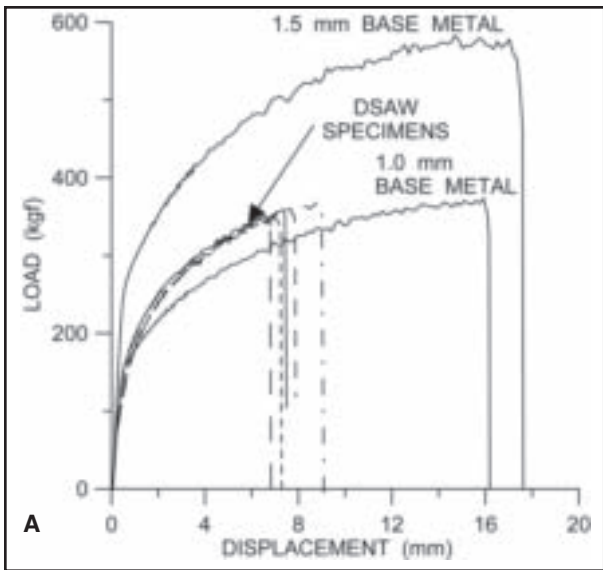


Fig. 14 — Load displacement curves from transverse tensile tests of welds produced with the following: A — 2.6kW total welding power at 20 mm/s welding speed; B — 4.2 kW at 60 mm/s.

wear, and the need for left- or right-handed tools during the blanking welding process (Ref. 2). Figure 2A shows a typical transverse section of a DSA weld produced between 1- and 1.5-mm-thick AA5182 sheets when the bottom two sheet surfaces were aligned during welding. There is significant drop-through due to the force of gravity acting on the weld pool during welding. Alternatively, Fig. 2B shows a transverse section of a weld produced with the top sheet surfaces aligned using the shims shown in Fig. 1. The drop-through and geometric discontinuity is significantly reduced. This is important for TWBs as surface and geometric discontinuities have been shown to negatively impact the formability of TWBs (Refs. 2, 32).  
 The Thermal Arc® PAW torch used in this study was originally designed for di-

rect current electrode negative (DCEN) PAW. The electrode for this torch is normally ground to a point with a 20-deg cone angle and setback into the orifice a specified distance as shown in Fig. 3A (Refs. 33, 34). However, Deutsch (Ref. 9) and Punkari (Ref. 11) reported excessive melting and formation of a molten metal bead at the electrode tip and very high rates of electrode tip degradation of the conical ground W-0.8% Zr electrodes when this torch was used for VPPA welding AA5182 and AA5754 aluminum alloy sheet. The significant changes in electrode tip geometry and arc length severely limited reproducibility between experiments. These same deficiencies were observed during the initial experiments in the present study. Figure 4 shows, for example, melting and balling that occurred on the tip of a ground W-0.8% Zr electrode after only 1 min of DSAW using 100-A peak current and 3-kW welding power.  
 Melting and formation of a molten ball on the electrode tip during manual AC or DCEP gas tungsten arc welding of aluminum alloys is common practice (Ref. 28); however, such large changes in electrode tip geometry is problematic during VPPAW due to the resultant changes in arc length, welding voltage, and power, as well as the close proximity of the orifice cup. In extreme cases, this can cause the electrode to short circuit against the PAW orifice cup, hindering further operation of

the welding torch. Overheating of the pointed electrode tip during VPPAW is largely due to the differences in energy balance between the electrode and workpiece during DCEN and DCEP portions of the variable polarity current waveform. During DCEN welding, approximately 70% of the total arc heat goes into the workpiece (the anode) and only 30% into the electrode (cathode) (Ref. 35). In this case, heating of the electrode is not sufficient to cause appreciable melting or thermal degradation of the electrode tip during DCEN PAW. This helps the electrode to maintain its initial shape and stabilizes the torch operating characteristics for long periods of operation. However, during VPPAW with a balanced AC waveform, an average of 50% of the arc heat is introduced into the anode and 50% into the cathode for each current cycle. As a result, the electrode tip can overheat and a molten ball of tungsten can form at the end of the initially pointed electrode.

It has been suggested that VPPAW should be performed with a blunt electrode to prevent melting and balling of the electrode tip (Refs. 36, 37). A blunt electrode tip increases the surface area interacting with the arc and improves the ability of the electrode to conduct heat away from the tip, thus extending the electrode life by preventing the formation of a molten ball during welding. However, as shown in Fig. 3B, the geometry of the blunt electrode required that the electrode setback be increased from 2.25 to 6.25 mm (+4 mm) to prevent direct contact between the electrode and PAW orifice cup. When welding with 100 A and 3 kW, this caused the welding voltage to increase from 32.1 to 38.7 V for a total increase in voltage of 6.6 V. Figure 5 shows the end of the blunt electrode after a

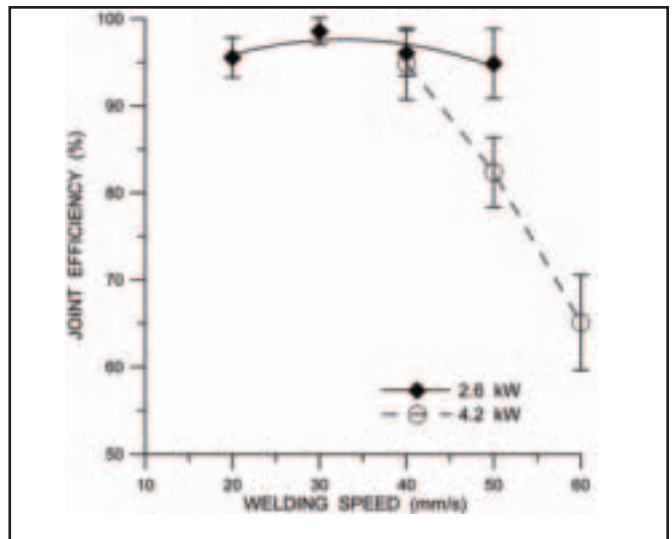


Fig. 15 — Joint efficiency vs. welding speed for specimens welded using total welding powers of 2.6 and 4.2 kW.

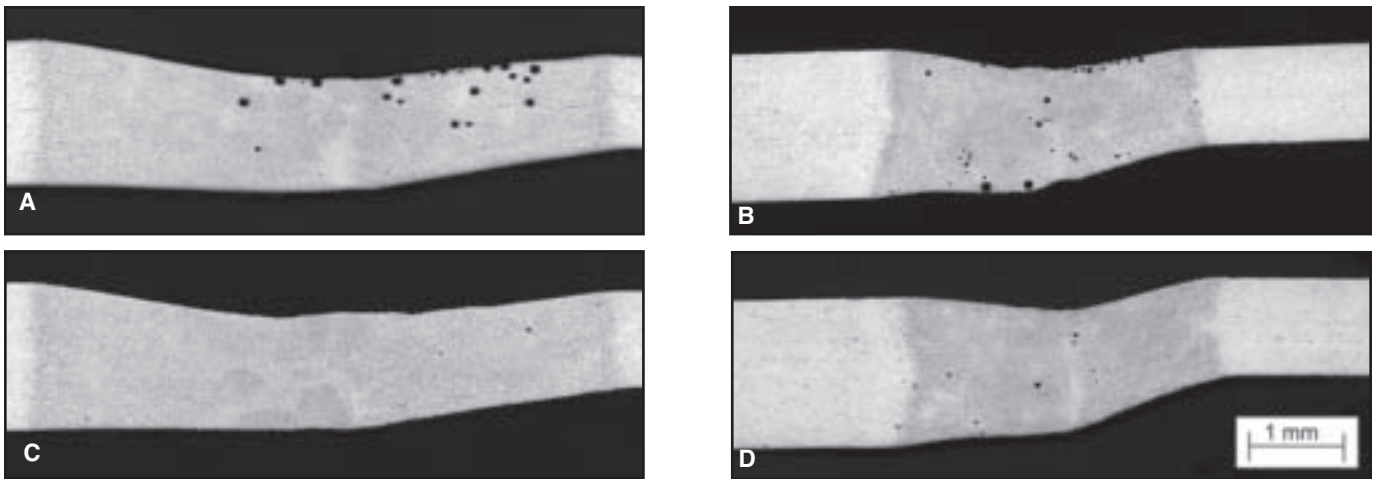


Fig. 16 — Hydrogen porosity in welds produced with a welding power of 3.0 kW at the following welding speeds: A — 30 mm/s; B — 50 mm/s; and stainless steel wire brushed specimens welded at C — 30 mm/s; D — 50 mm/s (etch: Keller's Reagent (Ref. 29)).

VPPA weld using 3-kW power. The blunt electrode had only a small molten spot indicating that the tip of the blunt electrode was much cooler than the tip of the pointed electrode. Also, there was no significant change in shape of the electrode tip geometry and arc length. Thus, the blunt electrode was found to be a superior geometry when using the PAW torch for variable polarity DSAW as it can be expected to provide repeatable and consistently reliable arc lengths and voltages for many welds.

The increased welding voltage associated with using the blunt electrode at a 6.25-mm setback was problematic, because the constant current power supply was designed to provide a maximum voltage of  $\pm 44$  V. Although the steady-state DSAW voltage was less than this limit, as shown in Fig. 6, the normal start-up transient voltage was observed to exceed 44 V and this caused the power supply to shut down. At the beginning of a DSA weld, as the sheets are initially fed between the two torches, there is a transition between the free-standing arc voltage and steady welding conditions. Kwon (Ref. 23) has shown that during this transition the welding arc initially wraps around the leading edge of the sheets, and the arc becomes longer and the arc voltage increases. Eventually, a maximum arc length and voltage is reached and the arc begins to couple with the workpiece. The voltage subsequently falls to the steady welding voltage as a stable weld pool is established. To eliminate the problem of the power supply cutting out during the start-up transient due to excessive arc length, an electrode ground to a 20-deg included angle and truncated to a 3.2 mm diameter was used. This geometry allowed the setback distance to be reduced to 5 mm, which in turn reduced the arc voltage sufficiently that the  $\pm 44$  V limit of the power supply was never exceeded during the initial transient. This

optimized electrode shape is compared to a blunt electrode in Fig. 5. A larger molten spot was created on the truncated electrode, but the melting was not sufficient to form a molten ball at the electrode tip and the electrode tip geometry was not substantially changed. This facilitated good consistency between results with minimal electrode degradation. Thus, 4.8-mm-diameter W-0.8% Zr electrodes ground to a 20-deg cone angle and truncated to a 3.2 mm diameter were used in the PAW torch throughout the remainder of this study.

#### Effects of Welding Speed and Power

To identify the range of acceptable welding conditions for joining 1.0- to 1.5-mm-thick AA5182 aluminum sheet, a series of welds were produced using the preset torch parameters shown in Table 1, total welding powers from 1.8 to 4.8 kW and welding speeds between 10 and 80 mm/s. The PAW and GTAW torches were centered over the joint. Prior to welding, the specimens were cleaned with acetone and methanol, but were not stainless steel wire brushed. Thus, oxide removal from the weld pool surface was entirely by cathodic etching from the arc.

The top weld surfaces of representative welds produced with 2.6-kW total welding power at welding speeds from 10 to 50 mm/s are shown in Fig. 7. The bottom weld

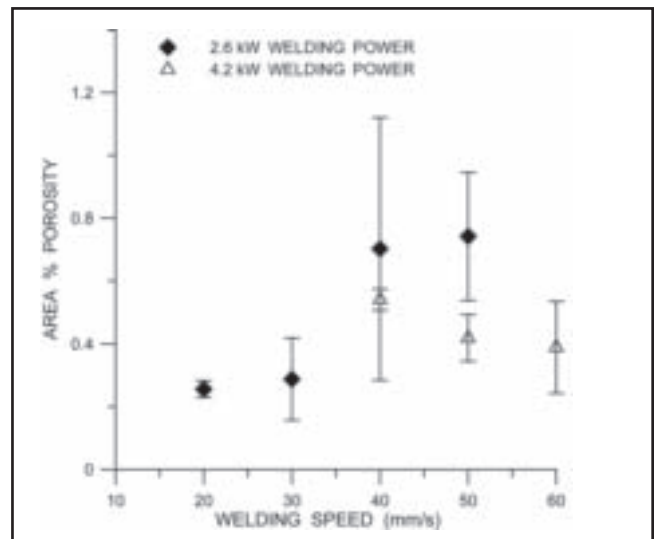


Fig. 17 — Weld metal porosity area fractions for weld specimens produced using total welding powers of 2.6 and 4.2 kW

bead surfaces were very similar in appearance. As shown in Fig. 7A, blowholes were produced when the welding speed was too slow or the welding power was too large. The mechanism for forming blowhole defects in DSA welded A5182 sheet is described in greater detail by Kwon (Ref. 23). Visually acceptable welds such as those shown in Fig. 7B were produced at higher welding speeds between 20 and 40 mm/s. As may be seen in Fig. 7C, welds produced at speeds greater than 50 mm/s were erratic with inconsistent arc coupling and cathodic cleaning of the oxide. In some locations, the original faying surface of the weld joint was not melted, resulting in incomplete fusion defects.

The weld bead surfaces of the welds produced in these experiments typically exhibited black patches along the weld centerline on the top and bottom weld surfaces — Fig. 7B, C. Leong et al. (Ref. 38)

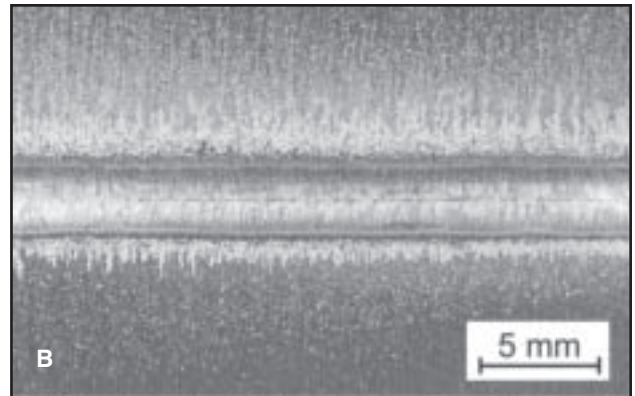
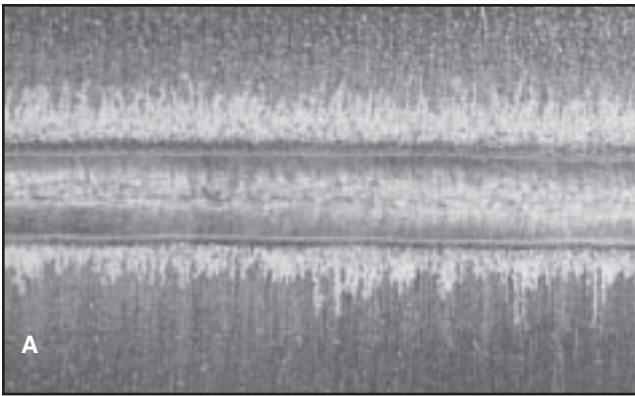


Fig. 18 — Top surfaces of welds produced on stainless steel wire-brushed specimens made using a constant power of 2.6 kW and welding speeds: A — 40 mm/s; B — 50 mm/s.

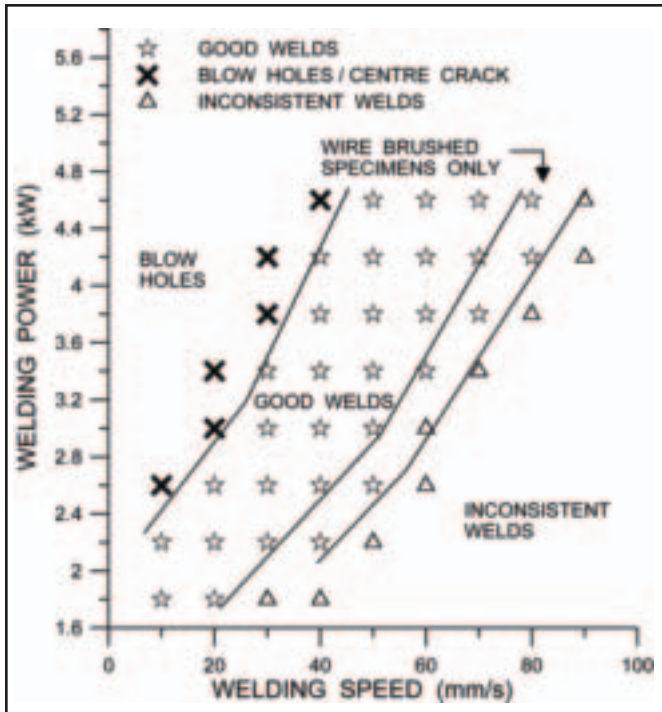


Fig. 19 — Range of welding conditions that produce visually acceptable welds on specimens that were stainless steel wire brushed prior to welding.

also reported similar formations. Using energy dispersive X-ray spectroscopy, they identified these regions to be rich in magnesium and oxygen. Thus, the black spots observed on weld surfaces in this study are believed to be magnesium oxides.

Cathodic etching of the oxide from the weld metal surfaces in the present study was similar to that observed in previous studies using VPPAW by Deutsch (Ref. 9) and Punkari (Ref. 11) and using DSAW by Kwon (Ref. 23). However, as shown in Fig. 8, the cathodically etched regions on the bottom GTAW torch side of the DSA welds produced in the present study using

of the thicker 1.5-mm sheet. As shown in Fig. 1, with the top surfaces of the sheets aligned in the clamping fixture, the bottom edge of the thick sheet is closer to the GTAW electrode creating a sharp corner and a shorter path for the current that attracts the welding arc and causes the arc and cathodic etching to favor the bottom surface of the thicker sheet. This effect was less pronounced on the top surface because the top sheet surfaces were flush during welding — Fig. 7B, C.

Figure 9 shows a representative transverse section of the weld shown in Fig. 7B. The weld bead geometry is very good with a small amount of underfill and drop-

dissimilar 1.0- to 1.5-mm-thick sheets were not symmetric. The cathodically etched region was generally wider and extended well into the base metal of the thicker 1.5-mm sheet. As may be seen in Fig. 8, however, cathodic cleaning of the oxide was incomplete on the bottom of the thinner sheet where segments of the original oxide were left floating on the weld pool surface at the fusion boundary.

The observed preferential cathodic etching of the thicker sheet surface is believed to be caused by attraction of the GTAW arc on the bottom surface to the protruding edge

through due to the effects of gravity acting on the weld pool during welding. All of the good DSA welds were symmetric, complete-joint-penetration welds with straight or slightly hourglass-shaped fusion boundaries. The welds exhibited epitaxial growth of columnar grains from the fine equiaxed base metal grains at the fusion boundary toward the center of the welds where there is a beneficial transition from columnar to equiaxed grains. This grain structure is similar to that reported previously by Kwon (Ref. 23) for DSA welded 1-mm-thick AA5182-O sheets.

The range of welding speeds and powers that produced visually acceptable DSA welds is shown in Fig. 10. In general, the welding speed increased with increased welding power. The maximum welding speed that produced acceptable welds was 70 mm/s when using 4.6 kW. For each welding power, a minimum welding speed was found to exist below which blowholes such as shown in Fig. 7A were created. Slightly lower heat inputs created excessively wide welds (greater than 10 mm) that frequently exhibited centerline cracks. As the welding speed was increased, visually acceptable welds were produced. The width of the good welds decreased as the welding speed was increased as a consequence of lower net heat input per unit distance during welding. A maximum welding speed was also found for each welding power above which inconsistent arc coupling was observed and erratic weld bead geometries and incomplete fusion defects such as shown in Fig. 7C were produced.

Figure 11 shows measured top and bottom weld widths of good welds vs. welding speed for welds made using two different welding powers, 2.6 and 4.2 kW. The top and bottom weld widths are almost the same for all welds. This is further indication that these welds were fully two dimensional with straight fusion boundaries through the sheets — Fig. 9. When using

2.6-kW welding power, the weld width decreased rapidly from 7 to 3 mm as the welding speed was increased from 20 to 50 mm/s due to decreasing heat input per unit distance. At a welding speed of 20 mm/s, the weld width was excessively large compared to the thickness of the specimens. The widths of the welds produced using 4.2-kW welding power were greater than those produced at 2.6 kW. Again, weld widths decreased to about 4 mm with increased welding speed. Inconsistent arc coupling and visually unacceptable weld beads were produced at speeds higher than those shown in Fig. 11.

Weld widths predicted using Kwon and Weckman's (Ref. 39) analytical heat transfer model of DSAW are also shown on Fig. 11. An average sheet thickness of 1.25 mm was assumed in the model and the thermophysical material properties used for the melting ratio calculations in Equation 1 were used. Following Kwon and Weckman (Ref. 39), the plasma arc distribution coefficient or arc radius,  $\sigma_{PP}$ , was assumed to be 1.8 mm and  $\sigma_{GP}$  for the GTAW torch was assumed to be 2.1 mm. The arc efficiencies of the PAW arc and GTAW arc,  $\eta_{PP}$  and  $\eta_{GP}$ , were adjusted until correlation between the measured weld widths as shown in Fig. 11 was obtained. In this case, correlation between measured and predicted weld widths was obtained when  $\eta_{PP} = 0.23$  and  $\eta_{GP} = 0.38$  were used. It should be noted that there are many simplifying assumptions used in an analytical heat transfer model such as this. Thus, while use of these values for arc distribution coefficients and arc efficiencies in the model facilitated correlation between the model predictions and experimentally measured weld widths, the actual values, may very well be somewhat different.

When using 2.6 kW, the maximum welding speed was predicted to be just above 50 mm/s. This is consistent with the measured results. At higher speeds, partial-penetration welds were predicted to occur. Above 60 mm/s, only heating of the sheets with no melting was predicted. When using 4.2 kW, welds produced at speeds greater than 60 mm/s exhibited inconsistent arc coupling. However, the analytical model predicted that complete-joint-penetration welds could be produced at significantly higher speeds up to about 85 mm/s before partial-penetration welds would be produced. This suggests that the actual welding speed was limited by the inability of the arc to cathodically clean the oxide at speeds greater than 60 mm/s.

Figure 12 shows plots of the melting ratio (see Equation 1) vs. welding speed and welding power. When using 2.6 kW, the melting ratio increased from 0.182 to a maximum value of 0.186 as speed increased from 20 to 30 mm/s. This is be-

**Table 2 — Comparison of Average Porosity Area Fraction Measured from Six Sections of Welds Produced on Specimens with and without Stainless Steel Wire Brushing Using a Total Welding Power of 3.0 kW**

Welding Speed	Surface Preparation	Average Porosity Area Fraction (%)
30 mm/s	Degreased	0.31 ± 0.15
30 mm/s	Degreased and SS wire brushed	0.05 ± 0.03
50 mm/s	Degreased	0.40 ± 0.07
50 mm/s	Degreased and SS wire brushed	0.09 ± 0.07

cause the time available for heat conduction into the sheets or the environment decreases as welding speed increases. However, as the welding speed increased beyond 30 mm/s, the melting ratio variations increased and the average value decreased to 0.166. This decrease was accompanied by incomplete oxide cleaning and intermittent coupling between the arc and the sheet. When using a total power of 4.2 kW, the maximum melting ratio was greater at 0.216. This maximum value occurred at the slowest acceptable speed of 40 mm/s and decreased as the speed increased due to increasing incomplete cleaning of the oxide and inconsistent arc coupling.

The theoretical maximum melting ratio value was predicted by Swift-Hook and Gick (Ref. 31) to be 0.48 for two-dimensional keyhole-mode laser beam welds with perfect coupling between the laser beam and the weld metal. The melting ratios measured in the present study of DSAW of AA5182-O aluminum sheet is less than half this theoretical value. This is likely due to the reduced arc efficiency of both arcs and heat loss due to conduction into the highly conductive aluminum sheets. Deutsch et al. (Refs. 9, 10) and Punkari et al. (Refs. 11, 12) found that the maximum melting ratio of single-beam Nd:YAG laser welded AA5182 alloy sheet was approximately 0.3 and was only 0.2 for dual-beam laser welds. They also found that the maximum melting ratios of VPPA welds made using the same PAW torch and power supply in AA5182 and AA5754 aluminum sheet of similar thickness was only 0.07 to 0.13 (Refs. 9, 11). They suggested that the stainless steel backing bar used during welding to control the underbead geometry acted as a large heat sink and that this was responsible for the lower melting ratios observed in their VPPA welds.

**Effects of Torch-to-Joint Alignment**

In laser beam welding of steel TWBs, the laser beam is sometimes offset toward the thicker sheet and beam weaving is used to promote additional melting of the thicker sheet. The additional molten

metal from the thicker sheet helps to provide a smoother transition from the thick to the thin sheet (Ref. 2). In the present study, therefore, a series of tests were carried out to evaluate the sensitivity and effects on the weld quality and bead geometry when the welding torches are offset from the joint centerline. A positive welding torch offset was used to indicate that the welding torches were offset toward the thicker sheet, a negative offset indicated the torches were offset toward the thinner sheet and a zero offset indicated that the torches were aligned with the joint. Five torch-to-joint configurations were used: -2 mm, -1 mm, 0, 1 mm, and 2 mm. Welds were made using 2.2-kW total welding power and speeds of 20, 24, and 30 mm/s to examine the effect of decreasing the heat input while varying the torch-to-joint alignment.

As shown in Fig. 13A, using a torch-to-joint alignment of -1 mm or more resulted in blowholes in the thinner sheet and little evidence of melting or cathodic cleaning of the oxide of the thicker sheet indicating that minimal heat transfer occurred to the thicker workpiece. Torch-to-joint alignments in the positive direction showed a slightly different trend. A torch offset of 0 or 1 mm produced acceptable quality welds such as shown in Fig. 13B. As shown in Fig. 13C, offsetting the torches even further to 2 mm or more resulted in porosity in the thicker sheet similar to those produced in the thinner sheet when using a negative offset. In this case, there was little evidence of melting or cathodic cleaning of the oxide of the thinner sheet.

The cause of the blowholes in the thick or thin sheets with positive or negative torch-to-joint alignment was initially suspected to be simply a result of applying excessive heat to the thicker or thinner workpiece; however, Kwon (Ref. 23) reported successful welding of 1- and 1.15-mm-thick sheet at the same welding powers and travel speeds. As a result, excessive heat input does not fully explain the presence of blowholes that was observed. It is thought instead that with the welding torches centered over the thin sheet (see Fig. 13A), there is insufficient cathodic cleaning of the oxide on the surface of the

thicker sheet and at the faying surfaces and, therefore, insufficient heat being transferred from the welding arc to the thick sheet. As the thin sheet starts to melt and form a molten weld pool, the uncleaned oxide at the faying surfaces prevents wetting and heat transfer through these oxide layers and into the colder thicker sheet. As a result, very little heat conduction occurs from the weld pool to the thick sheet. As all of the heat transferred from the arc into the surrounding sheets is now limited to conduction in only one transverse direction into the thinner sheet, the thinner sheet rapidly overheats causing an excessively wide weld pool and the formation of blowholes. As shown in Fig. 13C, when using a positive torch-to-joint alignment, failure of the arc to cathodically clean the oxide from the thinner sheet and faying surfaces also limits heat transfer into the thinner sheet, thereby causing overheating of the thicker sheet and formation of blowholes in the thicker sheet.

For the 1.0- to 1.5-mm sheet thickness ratio examined above, no noticeable benefit was observed by offsetting the welding torches from the joint. Offsetting the welding torches from the joint had a tendency to cause blowhole welding defects; however, slight offsets toward the thicker sheet of 1 mm or less were not detrimental to weld quality. The best weld quality was consistently obtained when the welding torches were aligned with the joint.

#### Metallurgical and Mechanical Properties of the DSA Welds

The 5000 series aluminum alloys derive their strength from solid-solution strengthening from the magnesium. Loss of magnesium due to preferential vaporization of the low vapor pressure Mg during laser welding of these alloys has been shown to result in a loss of strength (Refs. 13, 14). In the present study, discrete SEM-EDS measurements of composition were made at regular points along a line across the fusion zone of DSA welds produced at welding speeds of 20 and 50 mm/s using 2.6-kW total welding power and welding speeds of 40 and 60 mm/s when using 4.2-kW total welding power. Based on 36 measurements, the Mg content in the AA5182 base metal was  $4.53 \pm 0.30$  wt-% and based on 81 measurements, the Mg content in the fusion zones of the specimens was  $4.42 \pm 0.65$  wt-%. The differences observed between the mean base metal and the mean weld metal magnesium contents of each specimen were examined for a significant statistical difference using a t-test, at a 95% significance level, to test the null hypothesis that mean magnesium concentration was equal across both the base metal and fusion

zone. No significant difference between means was found using the t-test, which indicates that there is less than a 5% likelihood that a difference in Mg composition exists between the base metal and the fusion zone.

Vickers microhardness profiles across the DSA welds showed no noticeable difference in hardness between the base metal, heat-affected zone (HAZ), and weld metal. The microhardness ranged between 73 and 78 VHN. The lack of softening adjacent to the weld is not unusual for AA5182-O aluminum alloys as it is not considered to be a heat-treatable alloy (Ref. 26) and the sheets have been annealed and recrystallized (O-temper) prior to welding. The lack of magnesium loss and change in microhardness during DSAW of the AA5182-O aluminum alloy sheets is thought to be advantageous for TWB applications where the retention of weld metal strength is believed to be important for postweld forming (Refs. 40, 41).

Representative transverse tensile load-displacement curves for welds produced at total welding powers of 2.6 kW are shown in Fig. 14A. The yield and ultimate strengths of the DSA weld specimens generally approach the strength of the thinner base metal; however, the displacement to failure of the welded specimens was generally about 50% of the base metal displacements. As shown in Fig. 14B, the welds produced at 4.2-kW welding power and higher travel speeds of 50 and 60 mm/s showed equivalent yield strength, but there was a notable decrease in tensile strength due primarily to the significant reduction in displacement to failure. In all cases, tensile specimen failure was observed to occur in the weld near the fusion zone centerline. These results are not unlike those reported by Leong et al. (Ref. 38) for laser welded AA5182 sheet.

The joint efficiency has been used to compare the failure loads for welds produced under different welding conditions. In this study, the joint efficiency is defined as the failure load of the welded specimens as a percentage of the failure load for the thinner base metal. Joint efficiency results are presented in Fig. 15 for welds produced with constant powers of 2.6 and 4.2 kW. Joint efficiencies between 94 and 97% were attained by all welds produced at 2.6 kW. The joint efficiency of the welds produced at 50 and 60 mm/s using a welding power of 4.2 kW were significantly lower with the joint efficiency falling to 82 and 65%, respectively. As before, this decrease is attributed to the significant decrease in displacement to failure observed in these welds.

#### Hydrogen Porosity

Transverse sections of DSA welds produced under a variety of welding condi-

tions exhibited hydrogen porosity similar to that shown in Fig. 16A, B. Porosity in aluminum welds is generally known to be produced by hydrogen that is readily absorbed into molten aluminum during welding (Refs. 42, 43). Hydrogen may be introduced from water adsorbed on the base metal surface, from the hydrated oxide on the specimen surface or from moisture in the shielding gas (Refs. 28, 42, 43). As aluminum weld metal solidifies, any absorbed hydrogen is rejected from the solid into the liquid metal at the solid-liquid interface leading to nucleation and growth of hydrogen gas bubbles in the liquid. As may be seen in Fig. 16A, these bubbles will naturally try to float to the surface of the weld pool and escape into the atmosphere; however, at higher welding speeds, the weld may solidify before the hydrogen can escape or the oxide has not been completely removed from the weld pool surface and hydrogen is then trapped in the weld and gas pores are formed throughout the weld — Fig. 16B.

The volume fraction of porosity in the weld metal was inferred by measuring the area fraction of porosity on three transverse sections for each welding condition that tensile testing was performed on. As shown in Fig. 17, the average porosity levels ranged between 0.25 and 1.0 vol-% porosity for all of the welding conditions examined. No clear trends were identified between welding conditions as a great deal of scatter existed in the data; however, this scatter is not unexpected as metallographic porosity measurements do not consider the same proportion of a weld as density or radiographic testing methods (Ref. 44). Despite the scatter in the data collected, these porosity measurements did not exceed a threshold value of 1–2 vol-% porosity that has been shown to be the upper limit of porosity that can be tolerated in aluminum alloy welds without decreasing the strength of the weld metal (Refs. 45, 46). This is in close agreement with the tensile results obtained in this study where it was found that the joint yield strengths approached that of the thinner base metal sheet (see Figs. 14A and 15). Welds produced using a total welding power of 4.2 kW at 50 and 60 mm/s were the only exceptions. The cause for the decrease in weld strength at these welding speeds is not clear.

There are a number of standards and codes that place various limits on the porosity allowed in aluminum welds due to the impact porosity has on the strength of welds in static and dynamic loading. For example, the AWS D8.14M/D8.14:2000 specification for arc welded aluminum automotive components (Ref. 47) states that internal porosity must be <15% of the weld area. The porosity in the DSA welds shown in Fig. 17 is well below this value. In

AWS D1.2/D1.2M:2003, *Structural Welding Code — Aluminum* (Ref. 48), limits for porosity are based upon the number and sizes of pores evident in radiographic images of welds of specified size ranges. For welds made in 1.5-mm-thick sheet, the total pore area fraction must be less than about 2%. The porosity shown in Fig. 17 is well below this value. Finally, the CSA W59.2 standard for welded aluminum construction (Ref. 49) permits a maximum weld metal porosity of about 0.12% area fraction in radiographic images for applications using sheet material with a thickness of 3 mm or less. This tolerance is below the measured porosity contents shown in Fig. 17.

Weld metal ductility has been shown to be much less tolerant of porosity and can be reduced by very small amounts of porosity (Refs. 45, 50). Bayley and Pilkey (Ref. 32) have shown that even small amounts of porosity in aluminum TWBs reduces the strain to failure or formability of the welded blank by as much as 20%, as the onset of strain localization and failure was always predicted to occur at pores. Thus, the presence of hydrogen porosity in the DSA welds may explain the significant reduction in displacement to failure of the transverse tensile specimens (see Fig. 14).

Stainless steel wire brushing of aluminum specimens prior to welding has been proven to be effective in reducing the thickness of the oxide layer on the weld specimens with particular emphasis on removing hydrated oxides that have formed on the surfaces of this 5000 series alloy during extended storage periods (Refs. 28, 51). Two main benefits can be achieved: Hydrogen porosity can be significantly reduced, and the stability of the welding process can be increased (Refs. 25, 51). The reduction in porosity occurs as a result of removing the hydrated surface oxides that would otherwise dissociate in the welding arc and expose the weld pool to a source of hydrogen gas. The weld process stability arises from the reduction in cathodic cleaning that must take place to successfully remove the surface oxide and facilitate coupling between the arc and the weld metal. However, the need for cathodic cleaning is not eliminated by stainless steel wire brushing as the aluminum oxide will quickly form a thin new layer during the time lapse between brushing and welding.

#### Effects of Stainless Steel Wire Brushing Prior to Welding

To examine the effects of wire brushing on the weld quality and hydrogen porosity, a control study was performed to compare welds on specimens that had been stainless steel wire brushed prior to welding to those made on specimens that were not

brushed prior to welding. Two welding conditions were used: 3.0 kW at 30 mm/s and 3.0 kW at 50 mm/s. Six transverse cross sections were mounted for each weld condition, and the area fractions of porosity in the fusion zone were measured. Representative cross-sectional images are shown in Fig. 16C, D, and the average porosity area fractions measured from six transverse sections of each weld are summarized in Table 2. The results showed a decrease in hydrogen porosity of 84% and 77% for welds produced at 30 and 50 mm/s, respectively. The porosity content in stainless steel wire brushed specimens was not found to exceed the 0.12% limit specified by the CSA – W59.2 standard (Ref. 49) or other AWS standards and codes (Refs. 47, 48). These results suggest that stainless steel wire brushing prior to welding can be very effective for controlling hydrogen porosity formation during welding; however, it should be noted that the presence of hydrogen porosity was not eliminated entirely by wire brushing. The small amounts of hydrogen porosity observed could have been caused by small oxide particles that were entrapped into the soft aluminum alloy during brushing (Ref. 28), or from small amounts of hydrogen present in the base metal from prior processing (Ref. 51).

Visual weld quality of both the top and bottom weld beads was improved on specimens that had been stainless steel wire-brushed prior to welding. For example, the top weld surfaces of welds produced at 2.6 kW total welding power are shown in Fig. 18. These welds were produced at the same welding speeds and powers as the welds shown earlier in Fig. 7B, C. The stainless steel wire brushed specimens exhibit improved weld bead consistency compared to nonbrushed specimens. In addition, no surface contamination or black Mg oxide spots are present along the weld centerline on the wire-brushed specimens.

As was suggested previously by the analytical model predictions, the range of suitable welding conditions was also found to increase when stainless steel wire-brushing was used to remove the surface oxide from the workpieces prior to welding. This can be seen by comparing the top surfaces of welds produced at 2.6 kW and 50 mm/s in Figs. 7C and 18B. Without wire brushing, the welds exhibit an inconsistent top and bottom weld bead, while the welds produced at the same welding conditions show very consistent weld beads when the specimens were wire brushed prior to welding.

Figure 19 shows the increase in welding speeds found to produce visually acceptable welds on wire-brushed specimens. Wire brushing prior to welding facilitated an increase of welding speed of

about 20% for a given welding power. This is consistent with the predictions of the analytical heat transfer model shown previously in Fig. 11 where it appeared that the maximum welding speed for unbrushed weld specimens was limited by the ability of the arc to cathodically clean the surface oxide, rather than insufficient heat input to create a complete-joint-penetration weld pool. Consequently, the increased consistency of the weld bead at high welding speeds observed in this study is believed to be a result of mechanically removing the hydrated oxide layers prior to welding. This would reduce the amount of cathodic cleaning required to remove the surface oxide and help to maintain a stable weld pool when low-heat-input welding conditions are used.

There was no significant difference between the load vs. displacement curves obtained from transverse tensile tests and the resultant joint efficiencies of the unbrushed and brushed weld specimens. The results were similar to those presented earlier in Figs. 14 and 15 for weld specimens that were not brushed prior to welding. As before, the strength of the welds was similar to the thinner base metal sheet; however, the displacement to failure was about 50% of the base metal and this decreased to less than 20% of the base metal values as the welding speed was increased. In all cases, specimen failure occurred near the weld centerline.

The transverse tensile strength of welded aluminum alloys has been reported to be proportional to the loss in cross-sectional area of the weld caused by porosity (Refs. 46, 50) and to be tolerant of 1 to 2 vol-% porosity without having a noticeable effect on the joint strength (Ref. 45). For this reason, the similarity in strength observed between wire brushed specimens and nonbrushed specimens is not unexpected because the hydrogen porosity volumes were not found to exceed 1% porosity by volume (see Fig. 17 and Table 2). In this case, a slight improvement in strength would be expected from the reduction in porosity; however, the improvement in strength would not be expected to exceed 1% based on the maximum porosity levels observed in nonbrushed specimens. Consequently, the improvement in strength would not be expected to be evident considering the 2 to 5% variance in measurements from tensile testing of the welded specimens.

#### Conclusions

The feasibility of conduction-mode welding 1.0- to 1.5-mm-thick AA5182-O aluminum alloy sheet in the butt joint configuration for tailor welded blank applications using a new and novel double-sided arc welding (DSAW) process has been as-

essed. The balanced AC welding current used in this process was found to cause pointed W-0.8%Zr electrodes to melt and change tip geometry, electrode gap, and weld process conditions at excessively high rates due to the high arc heat input from the AC current. Flat or significantly truncated electrode tip geometries were found to be a superior geometry when using the PAW and GTAW torches for variable polarity DSAW as electrode tip melting is significantly reduced, thereby providing more consistent electrode tip geometry and repeatable and consistently reliable arc lengths and voltages for many welds.

Visually acceptable DSA welds could be produced in the 1.0- and 1.5-mm-thick AA5182-O sheets with good cathodic cleaning of the oxide from both the top and bottom surfaces of the weld bead over a wide range of welding speeds from about 10 mm/s when using 1.8-kW welding power to about 70 mm/s when using 4.6-kW welding power. These speeds are comparable to those reported possible when using VPPAW and are slightly lower than those reported for dual-beam Nd:YAG laser welding of these sheets. A zero torch offset from the weld joint was found to be optimal for the 1.0- to 1.5-mm-sheet thickness combination as this produced the most consistent and visually acceptable weld beads. The width of the DSA welds decreased with increased welding speed. In all cases, the maximum welding speed was limited by the onset of inconsistent arc coupling and cathodic cleaning of the oxide. Correlation between the measured weld widths and those predicted using an existing analytical thermal model of DSAW was possible provided reasonable values of the arc distribution coefficient and arc efficiency were used in the model for the PAW and GTAW arcs.

The melting ratio of this conduction-mode DSAW process was found to vary with process parameters, but a maximum value of about 0.216 was measured when using 4.6-kW welding power. This maximum value occurred at the slowest acceptable speed of 40 mm/s and decreased as the speed increased due to increasing incomplete cleaning of the oxide and inconsistent arc coupling.

The transverse tensile strengths of the DSA welds were found to be about the same as those of the thinner base metal sheet; however, in all cases, the displacement to failure was less, decreasing from about 50% of the thinner base metal sheet to less than 20% of the base metal as the welding speed was increased. In all cases, the specimens failed by fracture down the centerline of the welds. The overall joint efficiency of these DSA welds produced at the lower welding powers and speeds was as much as 97%, but this decreased to less than 85% as the welding power and speed

were increased primarily due to accompanying rapid decrease in displacement to failure.

Hydrogen porosity was observed in the weld metal even with cathodic cleaning of the oxide by the AC welding arc. The hydrogen porosity was significantly reduced by stainless steel wire brushing the weld surfaces prior to welding. This improved the consistency of the weld bead geometries and facilitated an increase in the maximum welding speed of about 20%; however, there was little or no change in the transverse tensile strengths with reduced hydrogen porosity.

The DSAW process has never before been applied to high-speed welding of two different sheet thicknesses such as is used in aluminum tailor welded blanks. It has a number of potential advantages over existing processes such as Nd:YAG laser beam welding and variable-polarity plasma arc welding. The DSAW process has been shown to provide cathodic etching of the aluminum oxide on both sides of the sheet, rather than just on the top side. The weld bead quality is as good as that possible on the top weld bead only of VPPA welds. This is beneficial to the formability and mechanical and fatigue strength of the welded blank. The weld bead is normally symmetrical through the sheet thickness. This can be expected to reduce the angular thermal distortion of the sheets that was observed in sheets welded using the VPPAW process. Finally, unlike Nd:YAG laser welding, there is no loss of Mg, weld metal strength, or hardness in the AA5182-O aluminum DSA welds. The significant potential advantages of the DSAW process with respect to the welding of aluminum tailor welded blanks may make DSAW the process of choice for such applications.

#### Acknowledgments

This research project was supported by the Natural Sciences and Engineering Research Council of Canada. The authors also wish to thank Frank Feng at Alcan International Inc., Kingston Research Laboratories now Novelis Global Technology Centre, Kingston, Ont., Canada, for supplying the AA5182-O project alloy sheet used in this study.

#### References

1. Kubel, E. 1997. Manufacturers want more tailored blanks. *Manufact. Eng.* 119(5): 38–45.
2. *ASM Handbook*, Vol. 14B, Metalworking: Sheet Forming. 10th ed. 2006. Materials Park, Ohio: ASM International, pp. 538–546.
3. Kazmier, R. J. 2001. Aluminum takes to the road. *Advan. Mater. Process.* 94(1): 42–44.
4. Das, S. 2000. Aluminum tailor welded blanks. *Advan. Mater. Process.* 157(3): 41–42.
5. Craig, E. 1998. The plasma arc process —

A review. *Welding Journal* 67(2): 19–25.

6. Huntington, C. A., and Eagar, T. W. 1982. Laser welding of aluminum and aluminum alloys. *Welding Journal* 62(4): 105-s to 107-s.
7. Duley, W. W. 1999. *Laser Welding*. Toronto, Ont., Canada: John Wiley & Sons.
8. Zhao, H., White, D. R., and DebRoy, T. 1999. Current issues and problems in laser welding of automotive aluminum alloys. *Int'l. Mater. Reviews* 44(6): 228–266.
9. Deutsch, M. 2001. Effects of Nd:YAG laser welding and VPPAW welding process variables on weld geometry and defects of 1.6 mm thick 5182 aluminum. MSc thesis, University of Waterloo.
10. Deutsch, M. G., Punkari, A., Weckman, D. C., and Kerr, H. W. 2003. The weldability of 1.6 mm thick AA5182 aluminum sheet by single and dual-beam Nd:YAG laser welding. *Sci. Technol. Weld. Join.* 8(4): 246–256.
11. Punkari, A. 2002. Variable polarity plasma arc welding and dual-beam Nd:YAG laser welding of aluminum alloys. MSc thesis, University of Waterloo.
12. Punkari, A., Weckman, D. C., and Kerr, H. W. 2003. Effects of magnesium content on dual-beam Nd:YAG laser welding of aluminum-magnesium alloys. *Sci. Technol. Weld. Join.* 8(4): 269–282.
13. Moon, D. W., and Metzbower, E. A. 1983. Laser beam welding of aluminum alloy 5456. *Welding Journal* 63(2): 53-s to 58-s.
14. Pastor, M., Zhao, H., Martukanitz, R. P., and DebRoy, T. 1999. Porosity, underfill and magnesium loss during continuous wave Nd:YAG laser welding of thin plates of aluminum alloys 5182 and 5754. *Welding Journal* 79(6): 207-s to 216-s.
15. Kutsuna, M., and Yan, Q. 1998. Study on porosity formation in laser welds in aluminum alloys (Report 1): Effects of hydrogen and alloying elements. *Welding Int'l.* 12(12): 20–32.
16. Zhang, Y. M., and Zhang, S. B. Nov. 23, 1999. Method of arc welding using dual serial opposed torches. U.S. Patent No. 5,990,446.
17. Zhang, Y. M., and Zhang, S. B. 1998. Double-sided arc welding increases joint penetration. *Welding Journal* 77(6): 57–61.
18. Zhang, Y. M., and Zhang, S. B. 1999. Welding aluminum alloy 6061 with the opposing dual-torch GTAW process. *Welding Journal* 78(6): 202-s to 206-s.
19. Zhang, Y. M., Pan, C., and Male, A. T. 2000. Solidification behavior of Al-Mg aluminum alloy using double-sided arc welding process. *J. Mater. Sci. Let.* 19: 831–833.
20. Zhang, Y. M., Pan, C., and Male, A. T. 2000. Improved microstructure and properties of 6061 aluminum alloy weldments using a double-sided arc welding process. *Metall. Mater. Trans. A* 31A: 2537–2543.
21. Zhang, Y. M., Pan, C., and Male, A. T. 2001. Welding of austenitic stainless steel using a double-sided arc welding process. *Mater. Sci. Technol. Weld. Join.* 17(10): 1280–1284.
22. Zhang, Y. M., Zhang, S. B., and Jiang, M. 2002. Keyhole double-sided arc welding process. *Welding Journal* 81(11): 249-s to 255-s.
23. Kwon, Y., and Weckman, D. C. 2008. Double sided arc welding of 5182 aluminum alloy sheet. *Sci. Technol. Weld. Join.* 13(6): 485–495.
24. Moulton, J. A. 2008. Double-sided arc welding of AA5182 aluminum tailor welded blanks. MSc thesis, University of Waterloo.
25. *ASM Handbook*, Vol. 2, Properties and

Selection: Nonferrous Alloys and Special Purpose Materials, 10th ed. 1990. Materials Park, Ohio: ASM International.

26. Smith, W. F. 1993. *Structure and Properties of Engineering Alloys*, 2nd ed., McGraw-Hill, Toronto, Ont., Canada.

27. Mossman, M. M., and Lippold, J. C. 2002. Weldability testing of dissimilar combinations of 5000 and 6000 series aluminum alloys. *Welding Journal* 81(11): 188-s to 194-s.

28. *Welding Handbook*, Vol. 3, Materials and Applications Part 1. 1996. Miami, Fla.: American Welding Society.

29. Vander Voort, G.F. 1999. *Metallography Principles and Practice*. Materials Park, Ohio: ASM International, pp. 510s and 610s.

30. ASTM Standard E8/E8M, 2008, *Standard Test Methods for Tension Testing of Metallic Materials*, ASTM Int'l., West Conshohocken, Pa., DOI: 10.1520/E0008/E0008M-08, [www.astm.org](http://www.astm.org), p. 3.

31. Swift-Hoof, D. T., and Gick, A. E. F. 1973. Penetration welding with lasers. *Welding Journal* 52(11): 492-s to 499-s.

32. Bayley, C. J., and Pilkey, A. K. 2005. Influence of welding defects on the localization behaviour of an aluminum tailor-welded blank. *Mater. Sci. Eng. A* 403: 1–10.

33. Reid, G. Oct. 2006. Personal communications. Thermal Arc, Ohio.

34. Thermal Arc WC100B *Plasma Torch*

*Manual*. 1983. Thermal Dynamics Corp., West Lebanon, N.H.

35. *Welding Handbook*, Vol. 2, Welding Processes, 9th ed. 2004. Miami, Fla.: American Welding Society.

36. Pistor, R. Nov. 2006. Personal communications. Liburdi Automation Inc., Dundas, Ont, Canada.

37. Dempsey, W. R., Bayless, E. O., and Clark, S. D. Dec. 9, 1986. Arc Welding Torch, U.S. Patent No. 4628177.

38. Leong, K. H., Sabo, K. R., Altshuller, B., Wilkinson, T. L., and Albright, C. E. 1999. Laser beam welding of 5182 aluminum alloy sheet. *J. Laser Appl.* 11(3): 109–118.

39. Kwon, Y., and Weckman, D. C. 2008. An analytical thermal model of conduction-mode double sided arc welding. *Sci. Technol. Weld. Join.* 13(6): 539-549.

40. Davies, R. W., Smith, M. T., Oliver, H. E., Khaleel, M. A., and Pitman, S. G. 2000. Weld metal ductility in aluminum tailor welded blanks. *Metall. Mater. Trans. A* 31A: 2755–2763.

41. Cheng, C. H., Chan, L. C., Chow, C. L., and Lee, T. C. 2005. Experimental investigation on the weldability and forming behaviour of aluminum alloy tailor-welded blanks. *J. Laser Appl.* 17(2): 81–88.

42. Kou, S. 2003. *Welding Metallurgy*, 2nd ed., Hoboken, N.J.: Wiley Interscience.

43. *ASM Handbook*, Volume 6 Welding,

Brazing and Soldering. 1993. Materials Park, Ohio: ASM International.

44. Saperstein, Z. P., Prescott, G. R., and Monroe, E. W. 1964. Porosity in aluminum welds. *Welding Journal* 40(10): 443-s to 453-s.

45. Ashton, R. F., Wesley, R. P., and Dixon, C. R. 1975. The effect of porosity on 5086-H116 aluminum alloy welds. *Welding Journal* 54(3): 95-s to 98-s.

46. Rudy, J. F., and Rupert, E. J. 1970. Effects of porosity on mechanical properties of aluminum welds. *Welding Journal* 49(7): 322-s to 336-s.

47. AWS D8.14M/D8.14:2000, *Specification for Automotive and Light Truck Components Weld Quality — Aluminum Arc Welding*. 2000. Miami, Fla.: American Welding Society.

48. D1.2/D1.2M:2003, *Structural Welding Code — Aluminum*. 2003. Miami, Fla.: American Welding Society.

49. CAN/CSA – W59.2-M1991, *Welded Aluminum Construction*. 1991. Toronto, Ont., Canada: Can. Standards Assoc., p. 40.

50. Shore, R. J., and McCauley, R. B. 1970. Effects of porosity on high strength aluminum 7039. *Welding Journal* 49(7): 311-s to 321-s.

51. Devletian, J. H., and Wood, W. E. Dec. 1983. Factors affecting porosity in aluminum welds — A review. *Welding Research Council Bulletin*. 290: 1–18.

## Nominations Sought for Honorary Meritorious Awards

The Honorary Meritorious Awards Committee makes recommendations for the nominees presented to receive the Honorary Membership, National Meritorious Certificate, William Irrgang Memorial, and the George E. Willis Awards. These honors are presented during the FABTECH International & AWS Welding Show held each fall. The deadline for submissions is December 31 prior to the year of the awards presentations. Send candidate materials to Wendy Sue Reeve, secretary, Honorary Meritorious Awards Committee, [wreeve@aws.org](mailto:wreeve@aws.org); 550 NW LeJeune Rd., Miami, FL 33126. Descriptions of these awards follow.

**William Irrgang Memorial Award.** Sponsored by The Lincoln Electric Co. in honor of William Irrgang, the award, administered by AWS, is given each year to the individual who has done the most over the past five years to enhance the Society's goal of advancing the science and technology of welding. It includes a \$2500 honorarium and a certificate.

**George E. Willis Award.** Sponsored by The Lincoln Electric Co. in honor of George E. Willis, the award, administered by AWS, is given each year to an individual who promoted the advancement of welding internationally by fostering cooperative participation in technology transfer, standards rationalization, and promotion of industrial goodwill. It includes a \$2500 honorarium and a certificate.

**Honorary Membership Award.** The honor is presented to a person of acknowledged eminence in the welding profession, or to one who is accredited with exceptional accomplishments in the development of the welding art, upon whom the Society deems fit to confer an honorary distinction. Honorary Members have full rights of membership.

**National Meritorious Certificate Award.** This certificate award recognizes the recipient's counsel, loyalty, and dedication to AWS affairs, assistance in promoting cordial relations with industry and other organizations, and for contributions of time and effort on behalf of the Society.

**International Meritorious Certificate Award.** This honor recognizes recipients' significant contributions to the welding industry for service to the international welding community in the broadest terms. The awardee is not required to be an AWS member. Multiple awards may be given. The award consists of a certificate and a one-year AWS membership.

# AWS Peer Review Panel

All papers published in the *Welding Journal's* Welding Research Supplement undergo Peer Review before publication for: 1) originality of the contribution; 2) technical value to the welding community; 3) prior publication of the material being reviewed; 4) proper credit to others working in the same area; and 5) justification of the conclusions, based on the work performed. The following individuals serve on the AWS Peer Review Panel and are experts in specific technical areas. All are volunteers in the program.

D. K. Aidun  
R. E. Avery  
M. Balmforth  
O. Blodgett  
J. E. M. Braid  
K. L. Brown  
P. Burgardt  
C. L. Chan  
Y. J. Chao  
B. A. Chin  
L. Connor  
G. E. Cook  
X. Deng  
P. J. Ditzel  
D. A. Fink  
G. W. Galanes  
D. L. Galiher  
Y. P. Gao  
J. A. Gianetto  
P. Hall  
D. L. Isenhour  
J. R. Jachna  
D. A. Javernick  
J. E. Jones  
A. Kar  
D. D. Kautz  
D. S. Kim  
P. J. Konkol  
J. J. Kwiatkowski  
L. Li  
M. V. Li  
M. Manohar  
A. F. Manz  
M. Marya  
K. Masubuchi  
J. Mazumder  
W. C. Mohr  
T. Morrissett  
P. E. Murray  
T. W. Nelson  
J. Peng  
M. Piltch

J. E. Ramirez  
B. Ridgway  
A. Ritter  
G. W. Ritter  
D. J. Rybicki  
E. F. Rybicki  
M. Sierdzinski  
T. A. Siewert  
H. Song  
C. D. Sorensen  
T. M. Sparschu  
W. J. Sperko

R. J. Steele  
H. Tang  
D. J. Tillack  
C. L. Tsai  
D. M. Vandergriff  
P. T. Vianco  
G. Wang  
M. Weir  
C. Y. Wu  
J. Xie  
Z. Yang  
S. Zhang

## Principal Reviewers

Y. Adonyi	D. Hauser	T. Mustaleski
C. E. Albright	P. Hochanadel	D. L. Olson
B. Alexandrov	T. Holverson	T. Palmer
S. S. Babu	J. E. Indacochea	W. Polanin
H. R. Castner	T. J. Kelly	M. Prager
M. Clark	M. Johnson	T. P. Quinn
M. J. Cola	D. Klingman	A. Rabinkin
C. E. Cross	D. J. Kotecki	R. W. Richardson
C. B. Dallam	S. Kou	C. Robino
B. Damkroger	R. Kovacevic	J. R. Roper
A. Debicari	D. Landon	M. Santella
T. DeRoy	K. Li	J. Scott
J. DeLoach Jr.	T. J. Lienert	H. B. Smartt
P. Dong	W. Lin	B. R. Somers
J. N. DuPont	J. C. Lippold	X. Sun
T. W. Eagar	S. Liu	M. Tumuluru
J. W. Elmer	M. Lucas	G. D. Uttrachi
D. F. Farson	H. W. Ludewig	P. Wang
Z. Feng	M. Ludwig	Y. P. Yang
S. R. Fiore	B. Madigan	G. Young Jr.
L. H. Flasche	R. Martukanitz	T. Zacharia
P. W. Fuerschbach	R. Menon	H. Zhang
W. F. Gale	R. W. Messler, Jr.	Y. M. Zhang
J. Gould	D. W. Meyer	Y. Zhou
D. A. Hartman	P. Michaleris	